Synthesis of Long T_1 Silicon Nanoparticles for Hyperpolarized ^{29}Si Magnetic Resonance Imaging

Tonya M. Atkins,[†] Maja C. Cassidy,[‡] Menyoung Lee,[§] Shreyashi Ganguly,[†] Charles M. Marcus,[§,⊥,*] and Susan M. Kauzlarich[†,*]

[†]Department of Chemistry, University of California, Davis, California 95616, United States, [‡]School of Engineering and Applied Science and [§]Department of Physics, Harvard University, Cambridge, Massachusetts 02138, United States, and [⊥]Center for Quantum Devices, Niels Bohr Institute, University of Copenhagen, 2100 Copenhagen Ø, Denmark

ABSTRACT We describe the synthesis, materials characterization, and dynamic nuclear polarization (DNP) of amorphous and crystalline silicon nanoparticles for use as hyperpolarized magnetic resonance imaging (MRI) agents. The particles were synthesized by means of a metathesis reaction between sodium silicide (Na_4Si_4) and silicon tetrachloride ($SiCl_4$) and were surface functionalized with a variety of passivating ligands. The synthesis scheme results in particles of diameter ~10 nm with long size-adjusted ^{29}Si spin−lattice relaxation (T_1) times (>600 s), which are retained after hyperpolarization by low-temperature DNP.
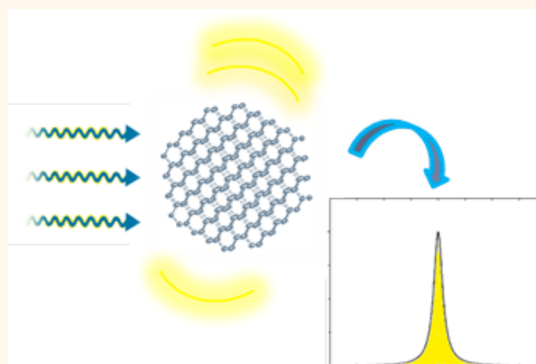
Silicon nanoparticles (Si NPs) with sizes ranging from 1 to 100 nm are of great interest across many research areas including thermoelectrics, photovoltaics, nanoelectronics, and nanomedicine. The smaller sizes (≤5 nm) emit light due to quantum confinement effects,[1−3] while larger sizes (≥ 10 nm) have desirable electronic transport properties and are pursued for the production of photovoltaics.[4,5] A variety of methods have been investigated for the production of Si NPs. Use of thermal techniques such as laser pyrolysis and thermal decomposition has been widespread,[1,6−10] but control over size and material properties using these methods is poor. Synthetic colloidal chemistry allows the simultaneous control of both the size and surface of the nanoparticle, offering prospects of creating large quantities of high-purity monodisperse Si NP samples. Previously, small (1−2 nm diameter) Si NPs have been prepared by the reaction of metal silicides with silicon tetrachloride.[11,12] The reaction of the Zintl salt with ammonium halide has also

been reported with average Si NP sizes of 4 nm.[13,14] Si NPs with a wide size distribution (1−20 nm) have also been prepared by a reverse micelle process both at ambient conditions and under high temperatures and pressures in a bomb.[15,16] Solution synthesis of Si NPs with diameters greater than 10 nm with discrete size distributions is challenging, and there are few examples reported in literature.[17,18] Recently, size control in the quantum confinement regime (≤5 nm) has been demonstrated through a combination of high-temperature treatment and etching with HF.[19] Alternative solution routes need to be explored to attain discrete size ranges for use in several applications.

Silicon and its oxide derivatives have emerged as materials of choice for applications in nanomedicine due to their biocompatibility and biodegradability *in vivo*[20,21] and are under investigation as drug delivery vehicles[22−26] and imaging agents.[27−33] Oxide derivatives, such as Stöber and fumed silicas, are not created equally, and toxicity has been shown to differ depending on the

* Address correspondence to
marcus@nbi.dk,
smkauzlarich@ucdavis.edu.

silica structure and is also dependent on the surface chemistry, reactivity, and NP morphology.[34] In vivo imaging of Si NPs has been achieved via a variety of techniques including optical imaging,[21,22,27,28] positron emission tomography (PET),[29] and magnetic resonance imaging (MRI).[35] MRI is an attractive technique for non-invasive imaging because it allows high-contrast imaging of opaque structures with detailed anatomical resolution without the use of ionizing radiation. In vivo MRI of Si NPs has previously been performed through the incorporation of paramagnetic materials[24,27,28] that disrupt the relaxation and coherence times of proximal ^{1}H nuclei, resulting in negative contrast or a lack of signal on a ^{1}H anatomical image. Recently, a new technique has been demonstrated for positive-contrast imaging of Si micron size particles using MRI[32,33] where the ^{29}Si nuclei within the Si particles (4.7% natural abundance) are hyperpolarized and imaged directly in vivo using ^{29}Si MRI. The body naturally contains very little silicon, so this technique allows for positive-contrast background-free imaging, similar to PET, but without the use of ionizing radiation. The initial demonstrations of ^{29}Si hyperpolarized MRI utilized commercially sourced micrometer-scale particles that could be monitored in the in vivo environment for over 40 min.[32] In intravenous studies, these particles were confined to the vascular structure of the animal, as their size rendered them unable to cross the cell wall.

At standard experimental temperatures and magnetic fields, the nuclear spin polarization is extremely low, on the order of one part in 10^{-5}–10^{-7} depending on the nuclear species. Hyperpolarization increases the nuclear spin polarization by several orders of magnitude, allowing the investigation of weak nuclear species by nuclear magnetic resonance (NMR) in low concentrations.[36] Hyperpolarization has been used in materials science as a nanoscale characterization tool,[37,38] while in biochemistry it has been used to reveal the structure of complex biomolecules such as proteins and peptides.[39,40] In clinical applications, hyperpolarized noble gases have allowed detailed imaging of the lung,[41] and metabolites such as ^{13}C-labeled pyruvate have been used for monitoring therapy in oncology.[42,43]

The spin–lattice relaxation time (T_1) sets the approximate time scale for which the signal from the hyperpolarized nuclei can be observed for imaging. Most enriched metabolites and noble gases have T_1 times on the order of 5–30 s in the in vivo environment, as the nuclei are strongly coupled to local ^{1}H spins.[41–43] Although a range of impressive in vivo experiments have been undertaken with these materials,[41–43] these times are at the very lowest of what is feasible for imaging clinically relevant biological processes. Extending the T_1 times of hyperpolarized tracers to >10 min would make a wide range of biological processes

accessible for imaging using the high specificity and resolution of MRI.

In solid-state spin-1/2 materials, such as Si, the primary source of nuclear spin–lattice relaxation is via an interaction with unbonded electrons or holes which occur in the form of free carriers or paramagnetic centers existing at lattice defect sites or at the surface. If the material is pure, the nuclear spin polarization is largely protected from sources of relaxation, resulting in bulk relaxation times of many hours.[32,36,44] Previous NMR investigations of Si micro- and nanoparticles showed that reducing the bulk toward the nanoscale results in T_1 times that are strongly dependent on the particle size, purity, and density of isolated defects.[32] The ^{13}C nucleus in diamond is another solid-state spin-1/2 system under investigation as a hyperpolarized imaging agent; however, to date, measured T_1 times have been extremely short, less than 2 s for particles 5–30 nm in diameter.[45]

The colloidal synthesis of Si NPs with average diameters of ~10 nm with room temperature T_1 times that exceed 600 s is described. The silicon nanoparticles were prepared from the metathesis reaction between sodium silicide (Na_4Si_4) and silicon tetrachloride ($SiCl_4$). While small (≤5 nm) NPs can be prepared by this route,[11,12,46] this work presents the larger NPs that can also be obtained from this reaction, isolated by means of product precipitation and density differences of the precipitate as outlined in the Experimental Methods section.[47,48] This results in particles that have significantly longer size-adjusted ^{29}Si nuclear spin relaxation (T_1) times than other commercially sourced Si particles,[32] as well as diamond nanoparticles of similar sizes.[45] We show that all of these particles can be hyperpolarized by low-temperature dynamic nuclear polarization (DNP), with polarization dynamics similar to the micrometer-scale Si particles previously investigated. These Si NPs are the smallest studied to date for hyperpolarization and, due to their size and long T_1 times, are promising for use as in vivo imaging agents that are small enough for intracellular studies and to cross the blood–brain barrier.[49]

RESULTS AND DISCUSSION

We used a metathesis reaction of sodium silicide (Na_4Si_4) with a silicon tetrachloride ($SiCl_4$) in each reaction for forming the chlorinated Si NPs (Figure 1).[11,12,46] The chlorinated Si NPs were then surface passivated with either an alkane or an aromatic amine by reacting them with the Grignard reagents, octylmagnesium bromide ($C_8H_{17}MgBr$) (Figure 1a) or 4-aminophenylmagnesium bromide (C_6H_6NMgBr) (Figure 1b), in dimethoxyethane (DME) or dioctyl ether (DOE)/squalane mixture. The ligands, octyl and aminophenyl, were chosen to provide both a nonpolar and polar surface group. Si NPs with average sizes of ~10 nm were isolated by collecting the portion of the precipitated product that remained at the
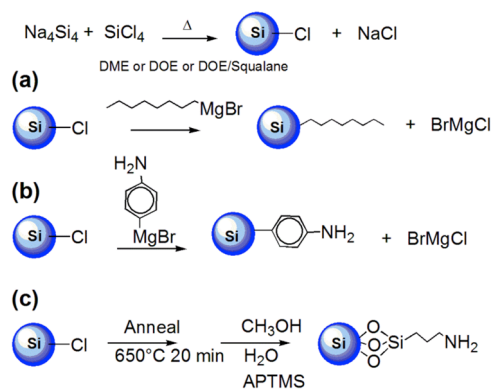
Figure 1. Synthetic schemes used to produce Si NPs. Each reaction starts with the reaction of the Zintl salt, Na_4Si_4, with $SiCl_4$ to form the chlorinated Si NPs, and then reacted with (a) octylmagnesium bromide, (b) 4-aminophenylmagnesium bromide, and (c) annealed and passivated with aminopropyltrimethoxysilane (APTMS).

interface between the water and organic layers. To enhance the crystallinity of the Si NPs, a third reaction was run (Figure 1c) where the chlorinated Si NPs were annealed in forming gas (95% Ar, 5% H_2) at 650 °C for 20 min and subsequently passivated with aminopropyltrimethoxysilane (APTMS).

Transmission electron microscope (TEM) images of Si NPs produced according to the schemes in Figure 1b,c are shown in Figure 2. Size distributions based on a number of images from these reactions are 10.3 ± 3.2 nm for the 4-aminophenyl-terminated Si NPs and 10.4 ± 4.4 nm for the annealed APTMS-terminated NPs. The images shown are representative of the products obtained according to the reactions outlined in Figure 1. The octyl-terminated Si NPs described by Figure 1a have a similar size and size distribution to that of the 4-aminophenyl-terminated NPs. All reaction schemes produced dispersed Si NP samples that suspend well in solution and were free from aggregation, indicating good termination of the particle surface. The annealed Si NPs showed a visible diamond crystalline lattice structure under high-resolution TEM (HRTEM) (inset, Figure 2b) and showed no additional aggregation after annealing due to sintering.

X-ray powder diffraction (XRD) and Raman spectroscopy were used to determine the degree of crystallinity of the as-grown and annealed particles (Figure 3). The metathesis reaction scheme consistently produced amorphous Si NPs, as determined by their negligible XRD signal (Figure 3a) and a Raman stretch of 497 cm^{-1} (Figure 3b), which is indicative of the broadened and shifted transverse optical Raman mode associated with amorphous silicon (see Supporting Information Table S1).[50] After annealing, strong XRD peaks were observed at positions agreeing with those corresponding to crystalline silicon standard, demonstrating that annealing provided a successful conversion from the amorphous to crystalline phase. The broadened and skewed Raman mode at 501 cm^{-1} was also consistent
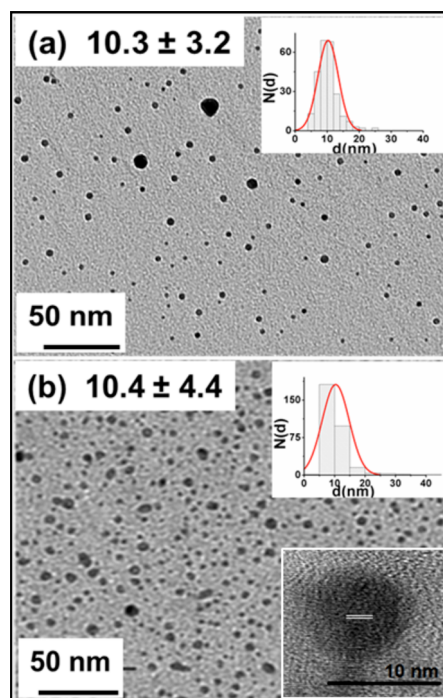

Figure 2. TEM images of Si NPs: (a) 4-aminophenyl-terminated and (b) annealed and passivated with APTMS. The size distributions are shown in the upper right inset. The lower right inset in panel b shows the crystallinity of the annealed Si NPs obtained using HRTEM. The lines in the lower right inset indicate the lattice fringes which give rise to the (220) lattice plane for diamond structured Si.

with models for crystalline Si NPs.[50] XRD peak analysis was used to determine the crystallite size. The average crystallite size from the Scherrer equation is 16.6 ± 3.0 nm, obtained from the three strongest diffraction peaks at 28.487, 47.395, and 56.194°. The average crystallite size obtained by XRD measurements is larger than the average particle size obtained by TEM analysis due to the differing preparation methods of the samples for analysis. XRD provides an average crystallite size of the entire powder samples, whereas the TEM grid is prepared from the sonicated solution. The larger NPs tend to precipitate rapidly, and therefore, the TEM grid presents a smaller average size than that observed by XRD.

The surface passivation for each of the samples was determined by infrared spectroscopy (Figure 4). The octyl-terminated Si NPs (Figure 4a) show stretches of the methylene groups at 2964 and 2891 cm^{-1}, together with a long chain methyl group observed at a wavelength of 796 cm^{-1}. The Si NPs passivated using 4-aminophenylmagnesium bromide show evidence of the amine group, indicated by a 3592 and 3517 cm^{-1} stretch, together with the N−H bend and the N−H wag at 1639 and 802 cm^{-1}, respectively (Figure 4b). For Si NPs that were terminated with APTMS, the weak secondary aliphatic amine stretch is observed at 3404 cm^{-1}, and the N−H bend and wag were observed at 1449 and 800 cm^{-1}, respectively. All samples showed
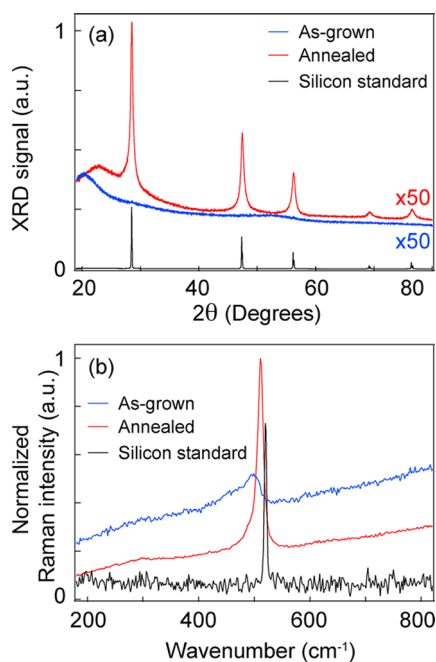
Figure 3. Crystallinity of as-grown and annealed Si NPs. (a) X-ray diffraction and (b) Raman spectroscopy of Si NPs before and after annealing show a transition from amorphous to crystalline states.

evidence of oxidation, indicated by the Si–O–Si stretch at $1000-1100 \, \text{cm}^{-1}$. This is typical for larger diameter Si NPs, as the decreased surface curvature reduces the surface coverage of the functional group. The frequency of the Si–O–Si stretch provides information of the structure of oxide layers as well as strain, porosity, and oxygen content,[51−53] and as the SiO_2 surface increases in thickness, the stretching mode band moves toward higher frequencies. The higher frequency of the Si–O–Si stretch observed for the alkyl-terminated Si NPs suggests a thicker oxide passivation for these particles compared to the APTMS-terminated Si NPs.

Figure 5 shows the measured ^{29}Si nuclear spin–lattice relaxation times (T_1) of a range of synthesized Si NPs with different diameters. The T_1 and sizes of Si nano- and microparticles measured in previous investigations are shown as a reference[32,33] together with a spin-diffusion-based model for T_1 relaxation.[33] The particles synthesized in this study show long T_1 times, ~600 s for the annealed samples, similar to T_1 times measured for particles ~60 nm in diameter also synthesized by wet synthesis techniques.[32] For high-purity Si particles, the primary mechanism for relaxation is spin diffusion of the nuclear polarization, P, from the center of the particle to the particle surface, according to

$$\frac{dP}{dt} = -D\Delta P \qquad (1)$$

where D is the spin diffusion constant, and so T_1 scales quadratically with particle diameter.[32,53,54] Unbonded electrons primarily at the silicon–silicon dioxide
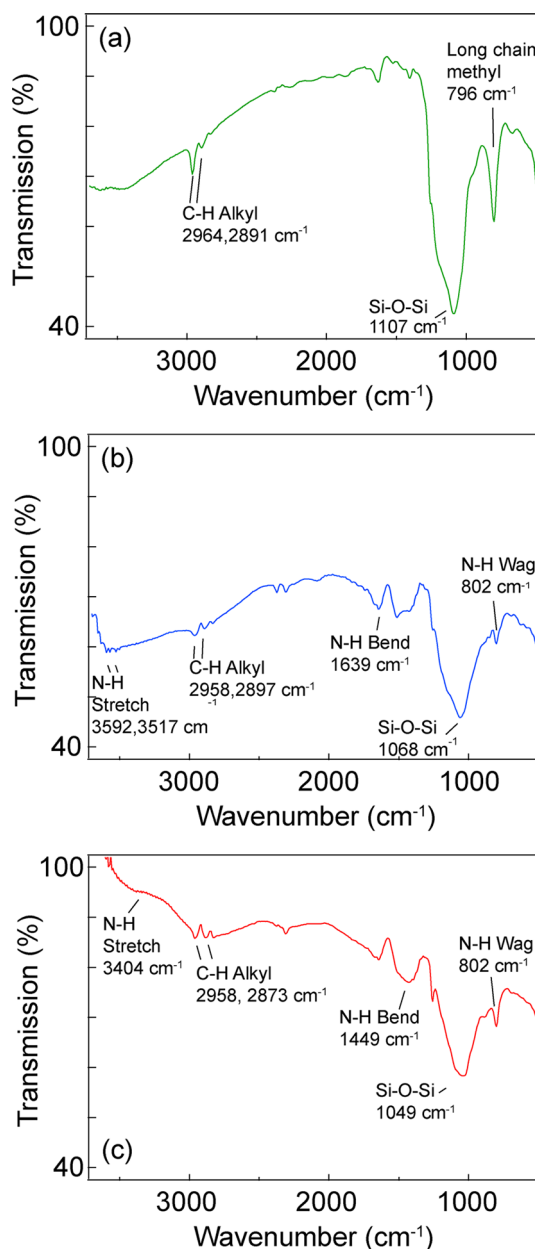

Figure 4. Infrared spectra of (a) octyl-terminated Si NPs, (b) 4-aminophenyl-terminated Si NPs, and (c) APTMS terminated Si NPs.

interface at the particle surface together with proximal spins contained within the passivating moiety can then drive local nuclear relaxation. The rate of this relaxation is set by the density of these spins and their own relaxation time and scales with distance r^{-6}, where r is the distance between the ^{29}Si nucleus and relaxing spin.[36] Impurities within the particle such as free carriers, unbonded electrons, or metal contaminants cause additional relaxation and shorten the ^{29}Si nuclear T_1 time.[32,53] Similar T_1 times were measured for the alkane- and aromatic-terminated particles, indicating that the choice of passivating moiety had little effect on the internal spin dynamics of the particle. We note that the T_1 times of the crystalline samples are shorter
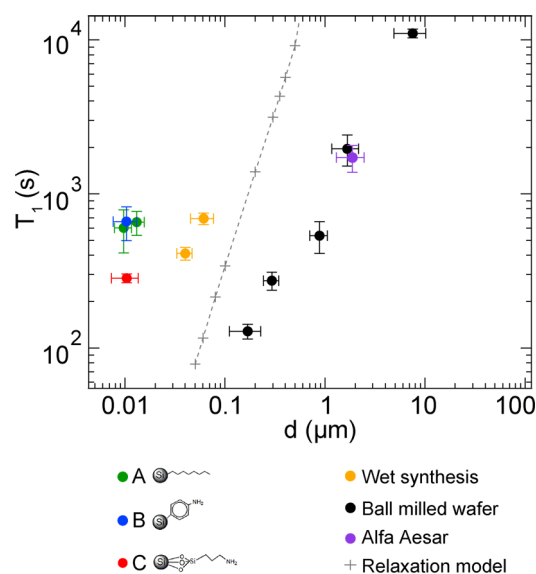
Figure 5. Nuclear spin relaxation (T_1) times at 2.9 T and 300 K as a function of particle diameter d for Si nanoparticles synthesized by schemes described in Figure 1. Previously reported T_1 measurements of other silicon particles are shown as a reference. Simulations of nuclear relaxation based on a spin diffusion model are also shown. Vertical error bars are from exponential fits to relaxation data; horizontal error bars are from size distributions.
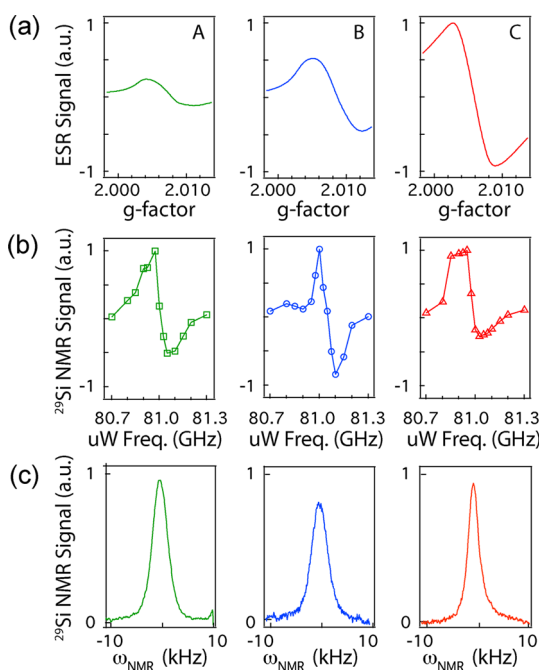

Figure 6. Electron spin resonance and dynamic nuclear polarization of (A) octyl-, (B) 4-aminophenyl-, and (C) APTMS-terminated Si NPs as indicated in the legend for Figure 5. (a) Electron spin resonance signal and (b) ^{29}Si nuclear polarization as a function of microwave frequency under DNP conditions. (c) ^{29}Si NMR spectra obtained under DNP conditions.

than the amorphous samples, potentially due to the introduction of isolated point defects in the silicon lattice brought about by the annealing process.

Natural oxidation of the surface of crystalline silicon creates a source of unbonded electrons that can be used for DNP.[55,56] Electron spin resonance (ESR) was performed to determine the nature of the defects and their density. Figure 6a shows the weight-adjusted ESR spectra (B = 0.35 mT, T = 300 K) for each reaction scheme, while the frequency response of the ^{29}Si nuclear polarization under DNP conditions (B = 2.89 T and T = 3.6 K) is shown in Figure 6b. For each sample, the ESR and DNP data are plotted across the same range of g-factors to aid in comparison. The g-factor extracted for each sample, as determined by the zero crossing in the ESR and DNP data, differs slightly (see Supporting Information Table S2), ranging from 2.0059 to 2.0087; however, there is good agreement seen between the room temperature ESR and low-temperature DNP data in each case. The defect density in these particles was lower than other particles previously investigated,[32,33] ranging from 4e^{12} to 4e^{13} cm^{-2} (see Supporting Information Table S2). The P_b defects, which occur due to an oxygen vacancy at the interface between crystalline silicon and silicon oxide, have a g-factor that is strongly anisotropic[56] and dependent on the orientation of the underlying crystalline lattice. For spherical nanoparticles, where one lattice orientation does not dominate over another, the orientation averaged g-factor for these defects is g = 2.006, which is in good agreement with the g-factor observed for our

crystalline samples. Both amorphous samples show similar g-factors in the range of 2.0078−2.0087. These are higher than the g = 2.005[57] and g = 2.0059[58] previously reported for bulk amorphous Si, potentially due to asymmetric strain.

All samples show a positive enhancement in nuclear polarization at microwave frequencies below the ESR frequency and negative polarization enhancements at frequencies above it, indicating that the polarization is generated by a dipolar interaction rather than a contact hyperfine interaction between the unbonded electrons and nearby ^{29}Si nuclei. The width of the DNP response is significantly narrower for the amorphous samples when compared to the crystalline samples, indicating that the polarization mechanism may be due to a single electron−single nucleus dipole−dipole interaction (commonly referred to as the solid effect)[36] for the amorphous samples, rather than a multielectron−single nucleus dipole−dipole interaction which occurs in the crystalline samples (commonly referred to as thermal mixing).[55] The ^{29}Si NMR spectra for the three samples after 3 h of DNP polarization are shown in Figure 6c. The amorphous Si NP samples show a broad resonance with a line width (full width at half-maximum) of ~3.6 kHz. The crystalline Si NP sample shows a slightly narrower resonance (line width ~2.2 kHz) shifted by ~600 Hz from the amorphous peak. Both line widths are broader than the ~500 Hz line width observed for bulk crystalline silicon[55] and 1.8 kHz
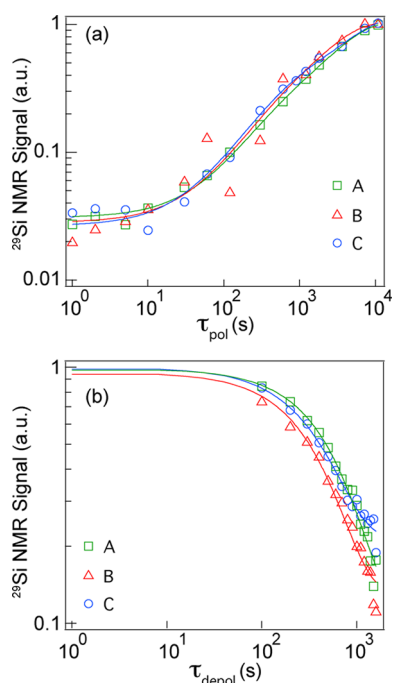
Figure 7. Time dependence of ^{29}Si polarization measured at 3.6 K in (A) octyl-, (B) 4-aminophenyl-, and (C) APTMS-terminated Si NPs synthesized according the scheme described in Figure 1. (a) ^{29}Si NMR signal as a function of polarization time τ_{pol}. (b) Depolarization of the ^{29}Si nuclear polarization at 3.6 K after 6 h of DNP. The solid lines show fits to the data described in the text.

line width observed for bulk amorphous silicon,[58] most probably due to strain.

The time evolution of the ^{29}Si nuclear polarization under DNP conditions for each of the samples is shown in Figure 7a. For each measurement, the microwave frequency was set to the peak value in Figure 6b before a saturation recovery sequence was performed and the ^{29}Si NMR signal measured with a single 90° pulse. All polarization curves are well fit by a biexponential function

$$P = P_\infty + (P_0 - P_\infty)(\alpha e^{(-t_{pol}/T_{1f})} + (1 - \alpha)e^{(-t_{pol}/T_{1s})}) \quad (2)$$

with a short time constant $T_{1f} \sim 400$ s and a longer time constant T_{1s} ranging from 3200 to 5700 s (see Supporting Information Table S3). Here, α corresponds to the fraction of nuclei that are being polarized directly *via* the dipole–dipole interaction and $(1 - \alpha)$ the fraction that are polarized indirectly *via* nuclear spin diffusion.

Both the amorphous samples show $\alpha = 0.13$, where for the annealed crystalline sample $\alpha = 0.23$, which is due to the higher concentration of unbonded electrons in this sample (see Supporting Information Table S2). Figure 7b shows the decay in ^{29}Si nuclear hyperpolarization measured at 3.6 K for each of the Si NP samples. The samples were polarized for 6 h with microwave irradiation at the peak value in Figure 6b, then the microwaves were turned off and the hyperpolarization was allowed to decay. The data are well fit by a single exponential

$$P = P_0 + (P_f - P_0)e^{(-t_{dep}/T_{1,dep})} \quad (3)$$

with all samples showing a depolarization time constant $T_{1,dep}$ greater than 300 s (see Supporting Information Table S3). The octyl-terminated Si NPs showed the longest depolarization time constant of ~600 s, consistent with the lower density of electronic defects observed. The long depolarization times of the amorphous Si NPs are surprising, as previous DNP investigations of Si microparticles composed of amorphous and crystalline silicon showed relaxation of the amorphous component within seconds after microwave irradiation ceased.[55]

CONCLUSION

We have successfully produced Si NPs having long ^{29}Si nuclear T_1 times with an average size of ~10 nm using a metathesis reaction of sodium silicide with a silicon tetrachloride. Combining these Si NPs with Grignard reagents resulted in particles that were partially passivated with alkyl and aromatic ligands. The partial surface passivation allows sufficient oxidation to provide hyperpolarization sites for DNP without compromising the nonaggregating characteristics of the sample. Additionally, the as-grown amorphous Si NP samples could be annealed into crystalline Si NPs that retained their nanoscale size and did not lead to larger aggregates due to sintering. Both the amorphous and crystalline Si NPs showed T_1 times more than 2 orders of magnitude larger than diamond nanoparticles of similar sizes and a 5-fold improvement on size-adjusted T_1 times when compared to silicon particles previously studied.[32] All Si NPs synthesized in this study could be hyperpolarized by low-temperature dynamic nuclear polarization and retained their polarization for >300 s, demonstrating that the long T_1 times of Si NPs persist down to the nanoscale.

EXPERIMENTAL METHODS

Chemicals. Silicon tetrachloride (SiCl$_4$, 99.998%) was purchased from Aldrich and was distilled. Sodium hydride powder (NaH, 95%) and silicon powder (Si, 99%) were purchased from Sigma-Aldrich and were used without further treatment. The aromatic halide 4-bromoaniline (C$_6$H$_6$BrN, 97%) and the alkyl halide octyl bromide (C$_8$H$_{17}$Br, 99%) were purchased from Aldrich and were used without further treatment. Tetraethylorthosilicate (TEOS,

99.999%) and poly(ethylene glycol) methyl ether (PEG) were purchased from Aldrich. Aminopropyltrimethoxysilane (APTMS, 97%) and dioctylether (DOE, 99%), dimethoxyethane (DME, 99%), and squalane (C$_{30}$H$_{62}$) were purchased from Aldrich. All manipulations were carried out under dry N$_2$, in either a glovebox or a Schlenk line, using standard anaerobic and anhydrous techniques.

Preparation of Na$_4$Si$_4$ Precursor. Sodium silicide, Na$_4$Si$_4$, was prepared according to a modified previously published procedure.[59]

A Spex 8000 M ball mill with a Spex tungsten carbide vial and two tungsten carbide balls (diameter of ~1 cm) were used to ball-mill mixtures of NaH and Si. The intimately mixed mixture of NaH and Si was placed into a 1 mL alumina crucible with a 1.5 mL alumina boat as a cover. The crucibles were placed into a quartz tube with stopcocks on both ends. The quartz tube was removed from the glovebox and placed in a horizontal tube furnace and connected to Ar flowing at 30 mL/min. The quartz tube was heated at 420 °C for 48 h. After the mixture was cooled to room temperature, a black solid was isolated and stored in a glovebox.

CAUTION: NaH and Na_4Si_4 are highly reactive to air and moisture and must be handled under an inert atmosphere.

Synthesis of Halide-Terminated Silicon NPs *via* Sodium Silicide with Silicon Tetrachloride. The Na_4Si_4 (1 mmol) and $SiCl_4$ (2 mmol) were placed into a three-neck 1000 mL round-bottom flask in a drybox. The solvent DME, DOE, or DOE/squalane was deoxygenated, and 400 mL of DME, DOE, or DOE/squalane was added to the starting reagents by a cannula. The solution was allowed to reflux overnight, and the solution was allowed to cool. The solvent was removed *via* short bridge under vacuum, and 200 mL of anhydrous THF was added to the Schlenk flask and stirred.

Synthesis of 4-Aminophenyl-Terminated Silicon NPs. To obtain 4-aminophenylmagnesium bromide (C_6H_6NMgBr), a Grignard reaction was performed by reacting 1.3 mol of 4-bromoaniline with 2 mol of magnesium and refluxed overnight. The Si NPs in THF were stirred, and 2.0 mL of 0.5 M C_6H_6NMgBr in tetrahydrofuran (THF) was added dropwise. The Grignard reagent was added over a 10 min period. The mixture was heated and allowed to reflux overnight. The reaction was allowed to cool, and the solution was separated by centrifugation (8000 rpm for 20 min). The liquid layer was decanted, and the solid was placed into a separatory funnel with a water hexane layer, and the suspended layer of solid between the water/hexane layer was isolated. The solid was washed three times with a total of 60 mL of methanol and centrifuged. The yield of product obtained was approximately 30%.

Synthesis of Octyl-Terminated Silicon NPs. To obtain octylmagnesium bromide, a Grignard reaction was performed by reacting 1.3 mol of octylbromide with 2 mol of magnesium and refluxed overnight. The Si NPs in THF were stirred, and 2.2 mL of 0.5 M octylmagnesium bromide ($C_8H_{17}MgBr$) in THF was added dropwise. The Grignard reagent was added over a 10 min period. The mixture was heated and allowed to reflux overnight. The reaction was allowed to cool, and the solution was separated by centrifugation (8000 rpm for 20 min). The liquid layer was decanted, and the solid was placed into a separatory funnel with a water hexane layer, and the suspended layer of solid between the water/hexane layer was isolated. The solid was washed three times with a total of 60 mL of methanol and centrifuged. A yield of approximately 30% was obtained.

Synthesis of Silicon NPs *via* Sodium Silicide with Silicon Tetrachloride, Annealing, and Aminopropyltrimethoxysilane (APTMS) Coating. The coating was a modified procedure previously published in literature.[60] The washed solid obtained from the synthesis of sodium silicide with $SiCl_4$ was placed into 5 mL of methanol and allowed to stir overnight. The solvent was evaporated by rotary evaporation and was annealed at 650 °C for 20 min under an 80:20 H_2/N_2 gas flow mixture in a flow furnace with a flow rate of 30 mL/min. The solid was placed back into fresh DME, and 5 mL of H_2O was added and allowed to stir overnight followed by the addition of 0.3 mL (1.8 mmol) of aminopropyltrimethoxysilane, and the resulting solution was stirred overnight. The solvent was evaporated under reduced pressure. The solid was washed with HPLC H_2O to remove any unreacted APTMS.

Characterization. Powder X-ray diffraction (XRD) data were collected using an airtight holder on a Bruker D8 diffractometer operating at 40 kV and 40 mA with Cu Kα radiation ($\lambda = 1.54184$ Å). Morphology and chemical functionality were analyzed by a CM-12 transmission electron microscope (TEM) with an accelerating voltage of 120 kV. Samples were ground with a 1:5 ratio of Si NP sample and anhydrous KBr, and diffuse reflectance was performed using a Shimadzu IR Prestige-21 Fourier transform infrared spectrophotometer (FTIR). High-resolution TEM (HRTEM) was performed on a JEOL 2500SE Schottky emitter microscope

operating at 200 kV and equipped with a Gatan multiscan camera. TEM samples were prepared by dissolving the silicon NPs into isopropyl alcohol and dipping the grids into the solution. For HRTEM, a drop of the solution was put on the copper grid and dried overnight under a heat lamp. Raman spectroscopy was performed on a Renishaw RM1000 laser Raman microscope equipped with a 514 nm argon laser for excitation guided by a microprobe.

Electron Spin Resonance. Continuous wave x-band electron spin resonance measurements were performed on the samples at room temperature (Bruker ElexSys E500). The ac field (amplitude 0.001 mT, $f_{mod} = 100$ kHz) was swept from 343.5 to 358.5 mT over a period of 60 s. An estimate of the electron spin concentration on the particle surface was made by taking ESR spectra with a piece of phosphorus-doped silicon wafer also inserted in the spectrometer cavity. The addition of the wafer piece resulted in the appearance of additional ESR signal due to the n-type doping. Comparing the peak areas and using the known doping level of the wafer piece (0.008−0.01 Ω·cm) yielded an order-of-magnitude estimate of the mean volume density of defect spins.

Room Temperature ^{29}Si T_1. The room temperature T_1 of the samples was measured at $B = 2.89$ T with a saturation recovery Carr−Purcell−Meiboom−Gill (CPMG) sequence. A train of 32 hard $\pi/2$ pulses saturated residual magnetization, and the sample was allowed to polarize for a time τ. The magnetization was rotated to the transverse plane with a single $\pi/2$ pulse and ($N = 200$) π pulses performed. The echos following each of the π pulses were Fourier transformed, and the height of the peak was used as a measure of the nuclear polarization. The data were fitted with an exponential function $P = P_0 + Ae^{-\tau/T_1}$, and the characteristic polarization time constant (T_1) was extracted.

^{29}Si Dynamic Nuclear Polarization. Low-temperature microwave-induced dynamic nuclear polarization (DNP) was performed at $T = 3.6$ K using a home-built DNP polarizer operating at $B = 2.89$ T, $f_{ESR} = 81$ GHz. Details of the polarizer construction are described in ref 33. A saddle coil that could be tuned across a wide range of temperatures was used for NMR detection. The ^{29}Si nuclear polarization was measured *in situ* under DNP using a saturation recovery sequence. A train of 32 hard $\pi/2$ pulses saturated residual magnetization, and the sample was allowed to polarize for a time τ. The magnetization was rotated to the transverse plane with a single $\pi/2$ pulse and the free induction decay measured. The area under the Fourier transformed peak was used as a measure of the ^{29}Si nuclear polarization. For depolarization measurements, the samples were polarized at the frequency giving the highest nuclear polarization for 6 h. The microwaves were then turned off, and the remaining ^{29}Si polarization was measured with a series of 20° pulses separated by 100 s. A mathematical correction was applied in post-processing to take into account the excess magnetization used up by earlier pulses in the sequence.

Conflict of Interest: The authors declare no competing financial interest.

Supporting Information Available: Image of suspended NPs, dynamic nuclear polarization, and electron paramagnetic resonance data. This material is available free of charge *via* the Internet at http://pubs.acs.org.

REFERENCES AND NOTES

1. Wilson, W. L.; Szajowski, P. F.; Brus, L. E. Quantum Confinement in Size-Selected, Surface-Oxidized Silicon Nanocrystals. *Science* **1993**, *262*, 1242–1244.
2. Ledoux, G.; Gong, J.; Huisken, F.; Guillois, O.; Reynaud, C. Photoluminescence of Size-Separated Silicon Nanocrystals: Confirmation of Quantum Confinement. *Appl. Phys. Lett.* **2002**, *80*, 4834–4836.

3. Cullis, A. G.; Canham, L. T.; Calcott, P. D. J. The Structural and Luminescence Properties of Porous Silicon. *J. Appl. Phys.* **1997**, *82*, 909–965.

4. Tian, B. Z.; Zheng, X. L.; Kempa, T. J.; Fang, Y.; Yu, N. F.; Yu, G. H.; Huang, J. L.; Lieber, C. M. Coaxial Silicon Nanowires as Solar Cells and Nanoelectronic Power Sources. *Nature* **2007**, *449*, 885–U8.

5. Pillai, S.; Catchpole, K. R.; Trupke, T.; Green, M. A. Surface Plasmon Enhanced Silicon Solar Cells. *J. Appl. Phys.* **2007**, *101*, 093105.

6. Heath, J. R. A Liquid-Solution-Phase Synthesis of Crystalline Silicon. *Science* **1992**, *258*, 1131–1133.

7. Werwa, E.; Seraphin, A. A.; Chiu, L. A.; Zhou, C. X.; Kolenbrander, K. D. Synthesis and Processing of Silicon Nanocrystallites Using a Pulsed-Laser Ablation Supersonic Expansion Method. *Appl. Phys. Lett.* **1994**, *64*, 1821–1823.

8. Zhang, Y. F.; Tang, Y. H.; Lam, C.; Wang, N.; Lee, C. S.; Bello, I.; Lee, S. T. Bulk-Quantity Si Nanowires Synthesized by SiO Sublimation. *J. Cryst. Growth* **2000**, *212*, 115–118.

9. Holmes, J. D.; Ziegler, K. J.; Doty, R. C.; Pell, L. E.; Johnston, K. P.; Korgel, B. A. Highly Luminescent Silicon Nanocrystals with Discrete Optical Transitions. *J. Am. Chem. Soc.* **2001**, *123*, 3743–3748.

10. Hessel, C. M.; Henderson, E. J.; Veinot, J. G. C. Hydrogen Silsesquioxane: A Molecular Precursor for Nanocrystalline Si−SiO$_2$ Composites and Freestanding Hydride-Surface-Terminated Silicon Nanoparticles. *Chem. Mater.* **2006**, *18*, 6139–6146.

11. Bley, R. A.; Kauzlarich, S. M. A Low-Temperature Solution Phase Route for the Synthesis of Silicon Nanoclusters. *J. Am. Chem. Soc.* **1996**, *118*, 12461–12462.

12. Mayeri, D.; Phillips, B. L.; Augustine, M. P.; Kauzlarich, S. M. NMR Study of the Synthesis of Alkyl-Terminated Silicon Nanoparticles from the Reaction of SiCl$_4$ with the Zintl Salt, NaSi. *Chem. Mater.* **2001**, *13*, 765–770.

13. Neiner, D.; Chiu, H. W.; Kauzlarich, S. M. Low-Temperature Solution Route to Macroscopic Amounts of Hydrogen Terminated Silicon Nanoparticles. *J. Am. Chem. Soc.* **2006**, *128*, 11016–11017.

14. Zhang, X. M.; Neiner, D.; Wang, S. Z.; Louie, A. Y.; Kauzlarich, S. M. A New Solution Route to Hydrogen-Terminated Silicon Nanoparticles: Synthesis, Functionalization and Water Stability. *Nanotechnology* **2007**, *18*, 095601.

15. Tilley, R. D.; Warner, J. H.; Yamamoto, K.; Matsui, I.; Fujimori, H. Micro-Emulsion Synthesis of Monodisperse Surface Stabilized Silicon Nanocrystals. *Chem. Commun.* **2005**, 1833–1835.

16. Wilcoxon, J. P.; Samara, G. A. Tailorable, Visible Light Emission from Silicon Nanocrystals. *Appl. Phys. Lett.* **1999**, *74*, 3164–3166.

17. Kim, H.; Seo, M.; Park, M. H.; Cho, J. A Critical Size of Silicon Nano-Anodes for Lithium Rechargeable Batteries. *Angew. Chem., Int. Ed.* **2010**, *49*, 2146–2149.

18. Bywalez, R.; Karacuban, H.; Nienhaus, H.; Schulz, C.; Wiggers, H. Stabilization of Mid-Sized Silicon Nanoparticles by Functionalization with Acrylic Acid. *Nanoscale Res. Lett.* **2012**, *7*, 76.

19. Hessel, C. M.; Reid, D.; Panthani, M. G.; Rasch, M. R.; Goodfellow, B. W.; Wei, J. W.; Fujii, H.; Akhavan, V.; Korgel, B. A. Synthesis of Ligand-Stabilized Silicon Nanocrystals with Size-Dependent Photoluminescence Spanning Visible to Near-Infrared Wavelengths. *Chem. Mater.* **2012**, *24*, 393–401.

20. Godin, B.; Gu, J. H.; Serda, R. E.; Bhavane, R.; Tasciotti, E.; Chiappini, C.; Liu, X. W.; Tanaka, T.; Decuzzi, P.; Ferrari, M. Tailoring the Degradation Kinetics of Mesoporous Silicon Structures through Pegylation. *J. Biomed. Mater. Res., Part A* **2010**, *94A*, 1236–1243.

21. Park, J. H.; Gu, L.; von Maltzahn, G.; Ruoslahti, E.; Bhatia, S. N.; Sailor, M. J. Biodegradable Luminescent Porous Silicon Nanoparticles for *In Vivo* Applications. *Nat. Mater.* **2009**, *8*, 331–336.

22. Tasciotti, E.; Liu, X. W.; Bhavane, R.; Plant, K.; Leonard, A. D.; Price, B. K.; Cheng, M. M. C.; Decuzzi, P.; Tour, J. M.; Robertson, F.; *et al.* Mesoporous Silicon Particles as a Multistage Delivery System for Imaging and Therapeutic Applications. *Nat. Nanotechnol.* **2008**, *3*, 151–157.

23. Tanaka, T.; Mangala, L. S.; Vivas-Mejia, P. E.; Nieves-Alicea, R.; Mann, A. P.; Mora, E.; Han, H. D.; Shahzad, M. M. K.; Liu, X. W.; Bhavane, R.; *et al.* Sustained Small Interfering RNA Delivery by Mesoporous Silicon Particles. *Cancer Res.* **2010**, *70*, 3687–3696.

24. Singh, N.; Karambelkar, A.; Gu, L.; Lin, K.; Miller, J. S.; Chen, C. S.; Sailor, M. J.; Bhatia, S. N. Bioresponsive Mesoporous Silica Nanoparticles for Triggered Drug Release. *J. Am. Chem. Soc.* **2011**, *133*, 19582–19585.

25. Mann, A. P.; Tanaka, T.; Somasunderam, A.; Liu, X. W.; Gorenstein, D. G.; Ferrari, M. E-Selectin-Targeted Porous Silicon Particle for Nanoparticle Delivery to the Bone Marrow. *Adv. Mater.* **2011**, *23*, H278.

26. Gu, L.; Park, J. H.; Duong, K. H.; Ruoslahti, E.; Sailor, M. J. Magnetic Luminescent Porous Silicon Microparticles for Localized Delivery of Molecular Drug Payloads. *Small* **2010**, *6*, 2546–2552.

27. Tasciotti, E.; Godin, B.; Martinez, J. O.; Chiappini, C.; Bhavane, R.; Liu, X. W.; Ferrari, M. Near-Infrared Imaging Method for the *In Vivo* Assessment of the Biodistribution of Nanoporous Silicon Particles. *Mol. Imaging* **2011**, *10*, 56–68.

28. Tu, C. Q.; Ma, X. C.; Pantazis, P.; Kauzlarich, S. M.; Louie, A. Y. Paramagnetic, Silicon Quantum Dots for Magnetic Resonance and Two-Photon Imaging of Macrophages. *J. Am. Chem. Soc.* **2010**, *132*, 2016–2023.

29. Tu, C. Q.; Ma, X. C.; House, A.; Kauzlarich, S. M.; Louie, A. Y. PET Imaging and Biodistribution of Silicon Quantum Dots in Mice. *ACS Med. Chem. Lett.* **2011**, *2*, 285–288.

30. Ananta, J. S.; Godin, B.; Sethi, R.; Moriggi, L.; Liu, X. W.; Serda, R. E.; Krishnamurthy, R.; Muthupillai, R.; Bolskar, R. D.; Helm, L.; *et al.* Geometrical Confinement of Gadolinium-Based Contrast Agents in Nanoporous Particles Enhances T-1 Contrast. *Nat. Nanotechnol.* **2010**, *5*, 815–821.

31. Singh, M. P.; Atkins, T. M.; Muthuswamy, E.; Kamali, S.; Tu, C.; Louie, A. Y.; Kauzlarich, S. M. Development of Iron-Doped Silicon Nanoparticles as Bimodal Imaging Agents. *ACS Nano* **2012**, *6*, 5596–5604.

32. Aptekar, J. W.; Cassidy, M. C.; Johnson, A. C.; Barton, R. A.; Lee, M.; Ogier, A. C.; Vo, C.; Anahtar, M. N.; Ren, Y.; Bhatia, S. N.; *et al.* Silicon Nanoparticles as Hyperpolarized Magnetic Resonance Imaging Agents. *ACS Nano* **2009**, *3*, 4003–4008.

33. Cassidy, M. C.; Chan, H.; Ross, B.; Marcus, C. M. *In-Vivo* Magnetic Resonance Imaging of Hyperpolarized Si Particles. Submitted for publication.

34. Zhang, H. Y.; Dunphy, D. R.; Jiang, X. M.; Meng, H.; Sun, B. B.; Tarn, D.; Xue, M.; Wang, X.; Lin, S. J.; Ji, Z. X.; *et al.* Processing Pathway Dependence of Amorphous Silica Nanoparticle Toxicity: Colloidal *vs* Pyrolytic. *J. Am. Chem. Soc.* **2012**, *134*, 15790–15804.

35. Louie, A. Y. Multimodality Imaging Probes: Design and Challenges. *Chem. Rev.* **2010**, *110*, 3146–3195.

36. Abragam, A. *Principles of Nuclear Magnetism*; Oxford University Press: New York, 1983; p p 144.

37. Wind, R. A.; Jones, H.; Little, M. J.; Hines, M. A. Orientation-Resolved Chemical Kinetics: Using Microfabrication To Unravel the Complicated Chemistry of KOH/Si Etching. *J. Phys. Chem. B* **2002**, *106*, 1557–1569.

38. Lelli, M.; Gajan, D.; Lesage, A.; Caporini, M. A.; Vitzthum, V.; Mieville, P.; Heroguel, F.; Rascon, F.; Roussey, A.; Thieuleux, C.; *et al.* Fast Characterization of Functionalized Silica Materials by Silicon-29 Surface-Enhanced NMR Spectroscopy Using Dynamic Nuclear Polarization. *J. Am. Chem. Soc.* **2011**, *133*, 2104–2107.

39. Bajaj, V. S.; Mak-Jurkauskas, M. L.; Belenky, M.; Herzfeld, J.; Griffin, R. G. Functional and Shunt States of Bacteriorhodopsin Resolved by 250 GHz Dynamic Nuclear Polarization-Enhanced Solid-State NMR. *Proc. Natl. Acad. Sci. U.S.A.* **2009**, *106*, 9244–9249.

40. van der Wel, P. C. A.; Hu, K. N.; Lewandowski, J.; Griffin, R. G. Dynamic Nuclear Polarization of Amyloidogenic Peptide Nanocrystals: GNNQQNY, A Core Segment of the Yeast Prion Protein Sup35p. *J. Am. Chem. Soc.* **2006**, *128*, 10840–10846.

41. Fain, S. B.; Korosec, F. R.; Holmes, J. H.; O'Halloran, R.; Sorkness, R. L.; Grist, T. M. Functional Lung Imaging Using Hyperpolarized Gas MRI. *J. Magn. Reson. Imaging* **2007**, *25*, 910–923.

42. Day, S. E.; Kettunen, M. I.; Gallagher, F. A.; Hu, D. E.; Lerche, M.; Wolber, J.; Golman, K.; Ardenkjaer-Larsen, J. H.; Brindle, K. M. Detecting Tumor Response to Treatment Using Hyperpolarized C-13 Magnetic Resonance Imaging and Spectroscopy. *Nat. Med.* **2007**, *13*, 1382–1387.

43. Golman, K.; Ardenaer-Larsen, J. H.; Petersson, J. S.; Mansson, S.; Leunbach, I. Molecular Imaging with Endogenous Substances. *Proc. Natl. Acad. Sci. U.S.A.* **2003**, *100*, 10435–10439.

44. Shulman, R. G.; Wyluda, B. J. Nuclear Magnetic Resonance of Si-29 in n-Type and p-Type Silicon. *Phys. Rev.* **1956**, *103*, 1127–1129.

45. Casabianca, L. B.; Shames, A. I.; Panich, A. M.; Shenderova, O.; Frydman, L. Factors Affecting DNP NMR in Polycrystalline Diamond Samples. *J. Phys. Chem. C* **2011**, *115*, 19041–19048.

46. Yang, C. S.; Bley, R. A.; Kauzlarich, S. M.; Lee, H. W. H.; Delgado, G. R. Synthesis of Alkyl-Terminated Silicon Nanoclusters by a Solution Route. *J. Am. Chem. Soc.* **1999**, *121*, 5191–5195.

47. Ma, X.; Wu, F.; Kauzlarich, S. M. Alkyl-Terminated Crystalline Ge Nanoparticles Prepared from Nage: Synthesis, Functionalization and Optical Properties. *J. Solid State Chem.* **2008**, *181*, 1628–1633.

48. Neiner, D.; Kauzlarich, S. M. Hydrogen-Capped Silicon Nanoparticles as a Potential Hydrogen Storage Material: Synthesis, Characterization, and Hydrogen Release. *Chem. Mater.* **2010**, *22*, 487–493.

49. Sonavane, G.; Tomoda, K.; Makino, K. Biodistribution of Colloidal Gold Nanoparticles after Intravenous Administration: Effect of Particle Size. *Colloids Surf., B* **2008**, *66*, 274–280.

50. Tripathi, V.; Islam, M. N.; Mohapatra, Y. N.; Cabarrocas, P. R. I. Raman Spectroscopy of Nano-structured Silicon To Study the Embedded Crystallites. *Eur. Phys. J.: Appl. Phys.* **2007**, *39*, 203–209.

51. Boyd, I. W. Deconvolution of the Infrared-Absorption Peak of the Vibrational Stretching Mode of Silicon Dioxide—Evidence for Structural Order. *Appl. Phys. Lett.* **1987**, *51*, 418–420.

52. Bange, J.; Patil, L.; Gautam, D. Growth and Characterization of SiO_2 Films Deposited by Flame Hydrolysis Deposition System for Photonic Device Application. *Prog. Electromagn. Res.* **2008**, *3*, 165–175.

53. Lee, M.; Cassidy, M. C.; Ramanathan, C.; Marcus, C. M. Decay of Nuclear Hyperpolarization in Silicon Microparticles. *Phys. Rev. B* **2011**, *84*, 035304.

54. Sen, P. N.; Thorpe, M. F. Phonons in AX_2 Glasses: From Molecular to Band-like Modes. *Phys. Rev. B* **1977**, *15*, 4030–4038.

55. Dementyev, A. E.; Cory, D. G.; Ramanathan, C. Dynamic Nuclear Polarization in Silicon Microparticles. *Phys. Rev. Lett.* **2008**, *100*, 127601-1-4.

56. Nishi, Y. Study of Silicon-Silicon Dioxide Structure by Electron Spin Resonance 0.1. *Jpn. J. Appl. Phys.* **1971**, *10*, 52.

57. Thomas, P. A.; Brodsky, M. H.; Kaplan, D.; Lepine, D. Electron Spin Resonance of Ultrahigh-Vacuum Evaporated Amorphous Silicon—*In Situ* and *Ex Situ* Studies. *Phys. Rev. B* **1978**, *18*, 3059–3073.

58. Lock, H.; Wind, R. A.; Maciel, G. E.; Zumbulyadis, N. Si-29 Dynamic Nuclear-Polarization of Dehydrogenated Amorphous-Silicon. *Solid State Commun.* **1987**, *64*, 41–44.

59. Ma, X. C.; Xu, F.; Atkins, T. M.; Goforth, A. M.; Neiner, D.; Navrotsky, A.; Kauzlarich, S. M. A Versatile Low Temperature Synthetic Route to Zintl Phase Precursors: Na_4Si_4, Na_4Ge_4 and K_4Ge_4 as Examples. *Dalton Trans.* **2009**, 10250–10255.

60. Zou, J.; Baldwin, R. K.; Pettigrew, K. A.; Kauzlarich, S. M. Solution Synthesis of Ultrastable Luminescent Siloxane-Coated Silicon Nanoparticles. *Nano Lett.* **2004**, *4*, 1181–1186.